nature COMMUNICATIONS

ARTICLE

Received 20 Jan 2016 | Accepted 3 May 2016 | Published 6 Jun 2016

DOI: 10.1038/ncomms11819 OPEN

111 oriented gold nanoplatelets on multilayer graphene as visible light photocatalyst for overall water splitting

Diego Mateo[1], Iván Esteve-Adell[1], Josep Albero[1], Juan F. Sánchez Royo[2], Ana Primo[1] & Hermenegildo Garcia[1]

Development of renewable fuels from solar light appears as one of the main current challenges in energy science. A plethora of photocatalysts have been investigated to obtain hydrogen and oxygen from water and solar light in the last decades. However, the photon-to-hydrogen molecule conversion is still far from allowing real implementation of solar fuels. Here we show that 111 facet-oriented gold nanoplatelets on multilayer graphene films deposited on quartz is a highly active photocatalyst for simulated sunlight overall water splitting into hydrogen and oxygen in the absence of sacrificial electron donors, achieving hydrogen production rate of 1.2 mol_{H2} per $g_{composite}$ per h. This photocatalytic activity arises from the gold preferential orientation and the strong gold–graphene interaction occurring in the composite system.

[1] Instituto de Tecnología Química, Universitat Politècnica de València-Consejo Superior de Investigaciones Científicas, Avenida de los Naranjos s/n, 46022 Valencia, Spain. [2] ICMUV, Instituto de Ciencia de Materiales, Universidad de Valencia, PO Box 22085, 46071 Valencia, Spain. Correspondence and requests for materials should be addressed to H.G. (email: hgarcia@qim.upv.es).

In the context of converting solar light into fuels there is a considerable interest in developing efficient photocatalysts for overall water splitting that could generate hydrogen in the absence of sacrificial electron donors under visible light ($\lambda > 400$ nm) irradiation[1–5]. Besides TiO_2 and other inorganic semiconductors[6], the use of graphenes (G) as additive or as photoactive component for the photocatalytic production of solar fuels is an active area of research[7–12]. G as photocatalyst offers the advantages of sustainability, when obtained from biomass[13–17], and the possibility of certain bandgap control either by doping or postsynthetic modification[18,19]. Graphitic carbon nitride (g-C_3N_4) is one of the most active photocatalysts based on a non-metallic semiconductor[20,21]. It has been reported that g-C_3N_4 containing a Pt as co-catalyst can generate hydrogen on solar light irradiation[22]. However, reports of hydrogen generation by Pt/G-C_3N_4 as photocatalyst use tertiary amines as sacrificial electron donors and, as far as we are aware, no overall water splitting with visible or solar light has been reported so far either for G or for G-C_3N_4 in the absence of sacrificial electron donors.

In the present manuscript we describe that 111 facet-oriented Au nanoplatelets supported on multilayer G ($\overline{Au}$/*ml*-G; $\overline{Au}$ meaning 111 facet-oriented Au nanoplatelets and *ml*-G meaning multilayer graphene) is an efficient photocatalyst for the overall water splitting in the absence of any additive reaching on simulated sunlight H_2 production rates about 0.9 mol_{H2} per $g_{composite}$ per h and apparent quantum yields of 0.08%. In addition, $\overline{Au}$/*ml*-G exhibits among the highest photocatalytic activity reported under visible illumination due to $\overline{Au}$ plasmon band excitation with a H_2 production rate above 100 $mmol_{H2}$ per $g_{composite}$ per h on ultraviolet-filtered simulated sunlight. In the case of TiO_2, it has been found that the lack of visible light photoresponse can be overcome by using Au nanoparticles (NPs) as light harvester and co-catalyst[23,24]. Strong evidence supporting that irradiation at the Au NP surface plasmon band introduces photocatalytic activity in TiO_2 was obtained from the coincidence of the absorption spectrum of Au/TiO_2 and photoresponse in the visible light[25]. Similarly, in the present case, a plasmon band photosensitization is observed for oriented $\overline{Au}$/*ml*-G. Evidence is presented supporting that the unprecedented photocatalytic activity of $\overline{Au}$/*ml*-G arises from the occurrence of a strong Au-G interaction derived from the unique features of the preparation procedure.

Results

Material preparation. $\overline{Au}$/*ml*-G films were prepared in a single step by pyrolysis at 900 °C under inert atmosphere of chitosan films of nanometric thickness containing $HAuCl_4$. Chitosan is obtained by deacetylation of natural chitin that is the main compound of insect and crustacean skins[26]. It has been previously found that chitosan forms uniform defect- and crack-free films of subnanometric rugosity on arbitrary substrates and that pyrolysis of these films result in the formation of single, few or multilayer G (ref. 27). Of relevance in the present case is also the known ability of chitosan and other biopolymers to adsorb metals in aqueous phase by complexation of the metal ions by the polysaccharide fibrils[28]. In the present case, $HAuCl_4$ was adsorbed on chitosan films on quartz before proceeding to the formation of G. Figure 1 summarizes the procedure followed for preparation of $\overline{Au}$/*ml*-G.

The Au content on *ml*-G film can be controlled in the range from ng to μg per cm^2 by varying the concentration of $HAuCl_4$ in the aqueous solution used for chitosan film impregnation from 10 to 1,000 μM. Methods section contains the exact amounts used in the preparation of the samples under study. Recently, the present procedure for the preparation of $\overline{Au}$/G has been reported by us[29]. Atomic force microscopy (AFM) measurements show that the thickness of the *ml*-G film of the samples under study is about 20 nm. The use of *ml*-G films is convenient to increase light absorption by G. It is known that single-layer G films have almost complete transparency (>99% transmittance), while the transparency decreases significantly for two layers (transmittance about 95%), four layers (transmittance about 85%) and multilayer (lesser transmittance). The present samples of $\overline{Au}$/*ml*-G are visually black films with metallic reflection.

For the sake of comparison besides $\overline{Au}$/*ml*-G at three Au contents, a sample of unoriented *Au*/*ml*-G was also prepared by polyol reduction method of Au(III) and subsequent adsorption of the resulting unoriented Au NPs on ml-G (*Au*/*ml*-G) obtained by exfoliation of carbon residue of chitosan powder after pyrolysis. Other sample for control purposes consisted in *ml*-G films on quartz prepared by 900 °C pyrolysis of chitosan films in the absence of $HAuCl_4$.

The Au content after pyrolysis of $\overline{Au}$/*ml*-G was determined by Au dissolution using aqua regia and subsequent quantitative inductively coupled plasma optical emission spectroscopy (ICP-OES) analysis of the resulting liquor, being the analytical data in good agreement with the values considering the complete adsorption by the chitosan film of the $HAuCl_4$ present in the impregnation step. As previously commented, the use of chitosan in water purification is based on its ability to adsorb metals from water[30,31]. For the present study, three $\overline{Au}$/*ml*-G films with Au content from 0.2 to 13.5 $\mu g_{Au}\,cm^{-2}$ were prepared.

Formation of *ml*-G in the pyrolysis process was confirmed by Raman and X-ray photoelectron (XP) spectroscopies, whose spectra coincide with earlier precedents[32]. Specifically, in Raman spectroscopy the graphitic (G) and defect (D) bands at about 1,600 and 1,350 cm^{-1} were also recorded for $\overline{Au}$/*ml*-G with I_G/I_D ratio of 1.13 (Supplementary Fig. 1). The XPS peaks of C 1s and Au 4f and their corresponding deconvolution showing the contribution of the individual components are presented in Fig. 2. The C1 s peak has a major component at 284.5 eV (86%) corresponding to graphenic carbons accompanied by minor contributions at 286.7 eV (13%) due to carbons containing oxygen atoms in their coordination. The presence of Au was also detected by XPS that shows the 4f peaks corresponding to Au(0) at binding energies of 85.5 and 89.09 eV (0.019 atomic %), appearing about 1.4 eV shifted to higher values with respect to the binding energy of bulk Au appearing at 84.1 and 87.7 eV confirming the strong interaction of the nanoparticles with the graphene support[33]. It is worth noting that despite the fact chitosan has been reported to render N-doped G after pyrolysis, no peak corresponding to residual N is observed in the XPS. This behaviour has been described before and has been attributed to the influence of the metal NPs-G interaction, which heals defects in G and, particularly, removes completely N atoms leaving a minor proportion of oxygenated functional groups[34].

The morphology and size of Au NPs was determined by field emission scanning electron microscopy (FESEM) and atomic force microscopy (AFM) images. The morphology of Au as nanoplatelets and their lateral dimensions ranging from 5 to 25 nm was established by counting a statistically relevant number of particles (Fig. 3). AFM allows determining with accuracy the height of the nanoplatelets between 2 and 4 nm (Supplementary Fig. 2).

The preferential 111 facet orientation of $\overline{Au}$/*ml*-G was confirmed by X-ray diffraction of the film (inset Fig. 4a). While Au NPs show five major diffraction peaks in X-ray diffraction (Supplementary Fig. 3), in the case of $\overline{Au}$/*ml*-G only the peaks corresponding to 111 and 222 diffractions are observed, indicating that these nanoplatelets have a preferential 111 facet orientation. The broad diffraction peak at 2Θ about 24° corresponds to the diffraction of *ml*-G. Further experimental

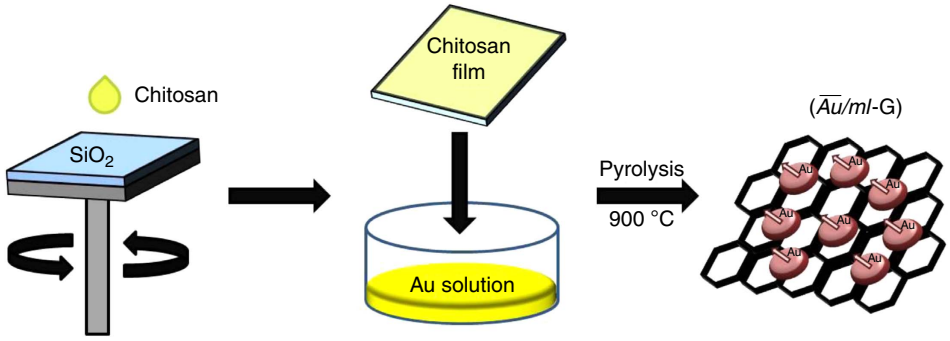

Figure 1 | Preparation of *Au*/*ml*-G films. The films were prepared by spin coating on clean substrate a chitosan solution that is subsequently immersed in $HAuCl_4$ solution and pyrolysis at 900 °C under inert atmosphere.

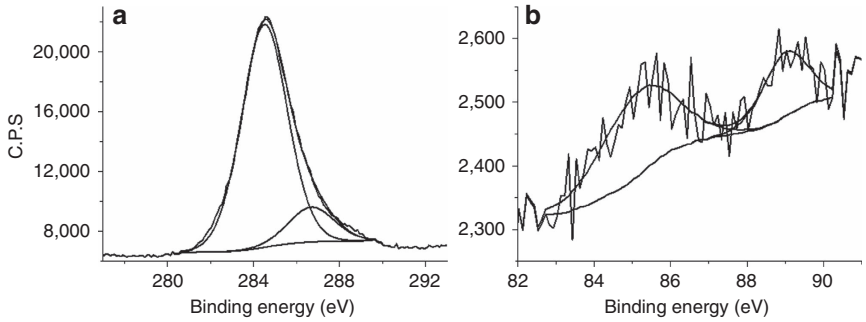

Figure 2 | XPS measurements. (**a**) C 1s peak showing the deconvolution into two types of C, graphenic and C bonded to oxygen, and (**b**) Au $4f_{7/2}$ and $4f_{5/2}$ peaks showing the presence of this element in the *Au*/*ml*-G surface.

evidence supporting the claim of 111 facet orientation was obtained by an electron backscattering diffraction (EBSD) technique in scanning electron microscopy (Fig. 4)[35,36]. In this case, orientation maps were collected by stepping the electron beam across the surface of the sample and indexing the resulting diffraction patterns. energy dispersive X-ray spectroscopy (EDX) image of *Au*/*ml*-G films shows the location of Au nanoplatelets and comparison of this image with that obtained by electron diffraction corresponding to the 111 diffraction shows a remarkable coincidence. Quantitative comparison of the EDX and 111 diffraction images using the ImageJ programme shows that about 90% of the particles present in the EDX image have 111 facet orientation.

Additional images supporting 111 facet orientation of Au nanoplatelets were obtained by transmission electron microscopy (TEM) after detaching the *Au*/*ml*-G films from the quartz substrates by mechanical polishing, dimpling grinding and final Ar ion bombardment (Supplementary Fig. 4). The images show the presence of Au as thin nanoplatelets. These nanoplatelets present preferential 111 facet orientation as shown by the electron diffraction pattern with the expected interplanar distance of 0.23 nm (ref. 37). High-resolution-TEM (HR-TEM) images (Supplementary Fig. 4b) show the presence of crystalline graphene.

Photocatalytic tests. Initial studies on the photocatalytic activity for H_2 generation of *Au*/*ml*-G were carried out by irradiating with a 300-W Xe lamp having quasi constant irradiance at all wavelengths in the ultraviolet and visible region (see Supplementary Fig. 5 for the lamp emission spectrum). *Au*/*ml*-G films coating a quartz square were placed on a sealed photoreactor (see also Supplementary Fig. 5 for a photoreactor photograph) and covered with an aqueous solution containing triethanolamine (TEOA) as sacrificial electron donor, observing the evolution of H_2 gas determined by micro-GC (see Methods section for experimental details). Figure 5 shows the temporal evolution of H_2 production rate in the presence of TEOA.

As it can be seen in Fig. 5, using TEOA as sacrificial electron donor agent the H_2 production rate decreases along the irradiation time, a fact that can be due to the decrease of TEOA concentration and by the accumulation of by-products derived from this tertiary amine that can act as light filters and/or photocatalyst poison. In the rest of the study, no sacrificial electron donor was used and all the experiments were performed using MilliQ water (pH 6).

Importantly, H_2 evolution was also observed in the absence of TEOA (see red line, Fig. 5), although the production rate was decreased by a factor of 5.5 times indicating that in the absence of TEOA the consumption rate of positive h^+ holes is the limiting kinetic step. In accordance with the absence of the sacrificial electron donor, besides H_2, evolution of O_2 was also observed in the absence of TEOA at a rate that agrees with the expected stoichiometry for overall water splitting, with some differences at short irradiation times. This deviation from the 2:1 stoichiometry has been previously observed in the literature and attributed to changes in the oxygen content of the photocatalyst or to oxygen adsorption on the photocatalyst[38]. It could also be that the presence of some minor impurities acting at initial irradiation times as sacrificial electron donors could be at the origin of this misbalance that is not observed as the reaction progresses. In the absence of sacrificial electron donor, H_2 production rate along the irradiation time was varying from 1.2 to 1 mol_{H2} per $g_{composite}$ per h in 24 h. The main decrease in H_2 production rate took place during the first 5 h of irradiation; afterwards, the production rate remained practically constant within 24 h. Similar behaviour can

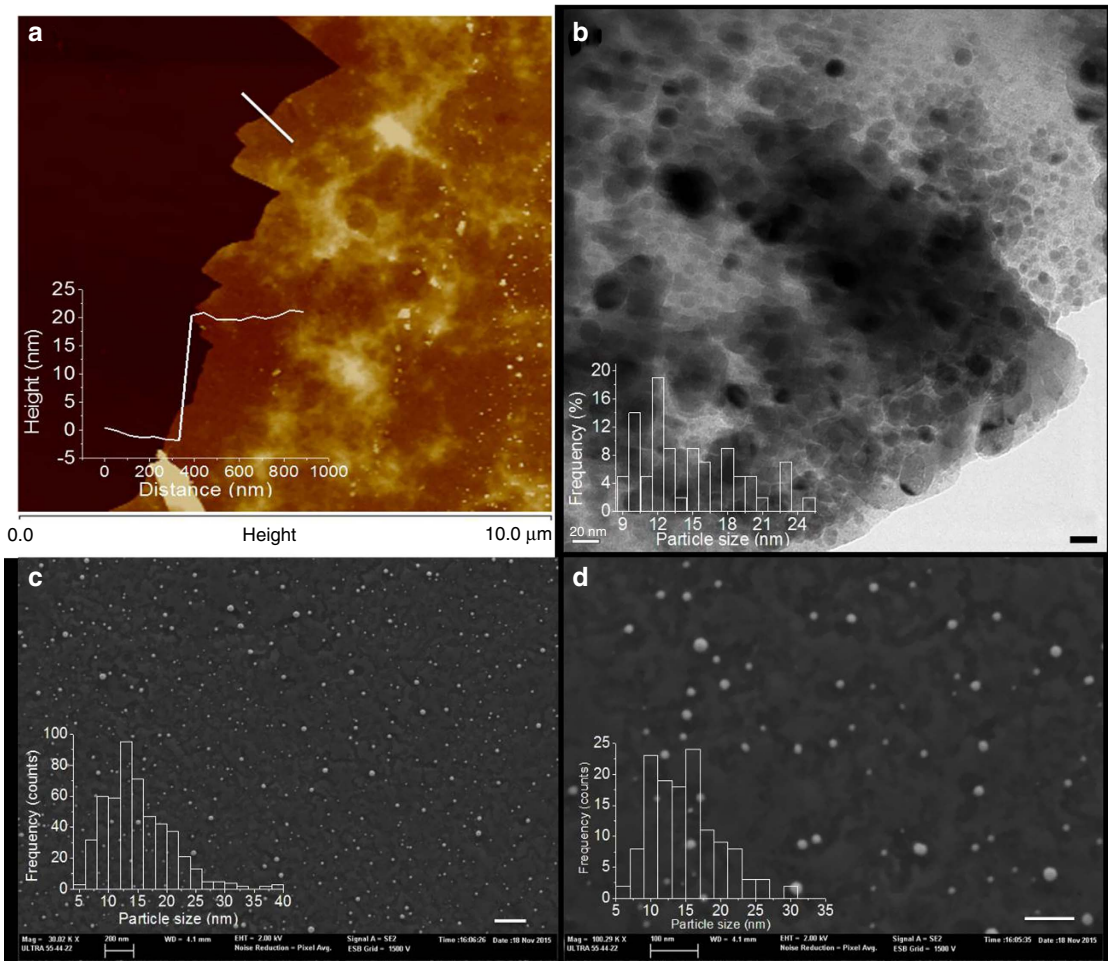

Figure 3 | $\overline{Au}$/ml-G images. AFM frontal view (**a**), TEM micrograph (scale bar, 20 nm) (**b**) and FESEM images (scale bar 20 nm) at two different magnifications (**c**,**d**) of a $\overline{Au}$/ml-G film (1 µg Au per cm^2) (scale bars of 200 and 100 nm for **c** and **d**, respectively). Inset in **a** shows the thickness of the *ml-G* film across the white line, while insets in **b**–**d** are the histograms showing Au nanoplatelet lateral size distribution.

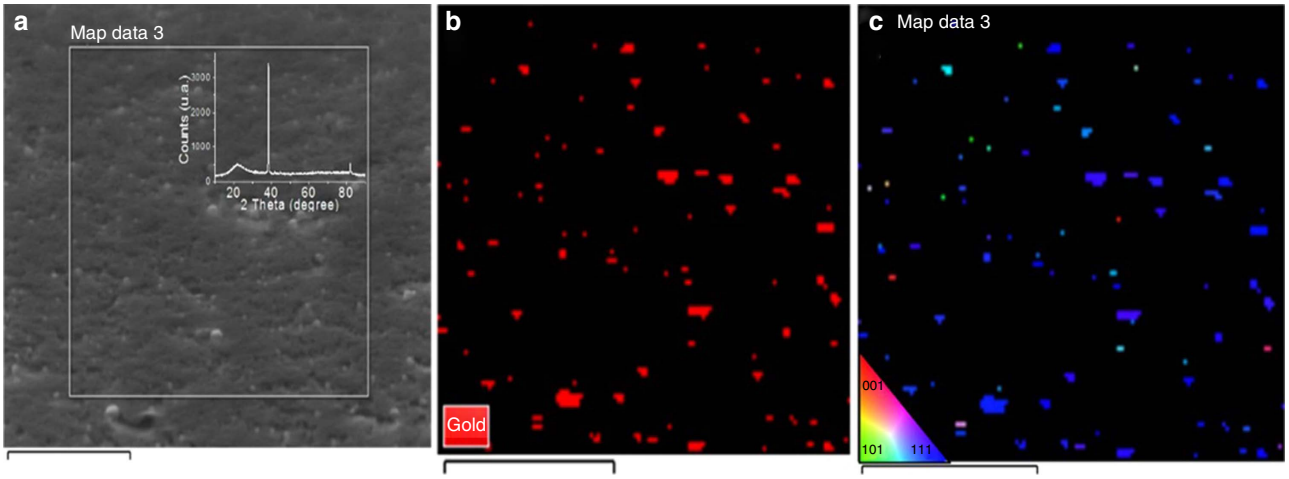

Figure 4 | Electron microscopy images of $\overline{Au}$/ml-G. (**a**) FESEM image of $\overline{Au}$/ml-G. (**b**) EDX image of the square indicated in the left FESEM image mapping the presence of Au. (**c**) Image of Au nanoplatelets showing 111 facet orientation in blue (scales bar, 500 nm in all cases). The inset shows the colour codes corresponding to other facet orientations. Scale bars, 500 nm.

be observed for the ultraviolet-filtered measurement (Fig. 5, green line). This relatively minor decrease in the photocatalytic activity in 24 h could be due to deactivation by the presence in the photoreaction of some O_2. Since the overall water splitting produces simultaneously H_2 and O_2, the quenching due to the residual presence of O_2 at initial irradiation times is low and does not interfere in the reaction. However, at longer times, increasing amounts of residual O_2 remaining in the photoreactor could inhibit partially the H^+ reduction until a stationary production is reached.

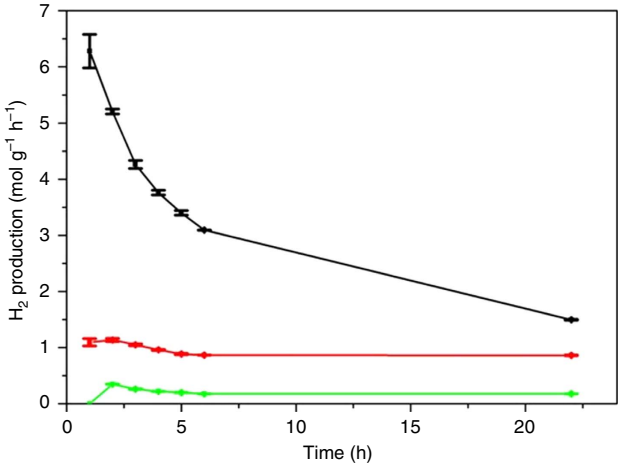

Figure 5 | Temporal evolution of hydrogen production rate. Experiments were carried out under ultraviolet–visible irradiation in the presence (black line) and in the absence (green and red lines) of TEOA as sacrificial agent using a 2 × 2-cm^2 $\overline{Au}$/*ml*-G film (Au content 1 μg cm^{-2}, total photocatalyst mass including *ml*-G 4.25 μg cm^{-2}). The red line corresponds to the experiment in the absence of TEOA without any filter, while the green line was obtained irradiating through an ultraviolet cutoff filter. The plots show the H_2 production with the estimated errors (calculated as the square root of the sum of (a-ā)^2, being a the value of the data set and ā the mean of the data set, divide by the number of data points) referred to the total Au plus *ml*-G photocatalyst amount (see Methods section for the estimation of *ml*-G weight).

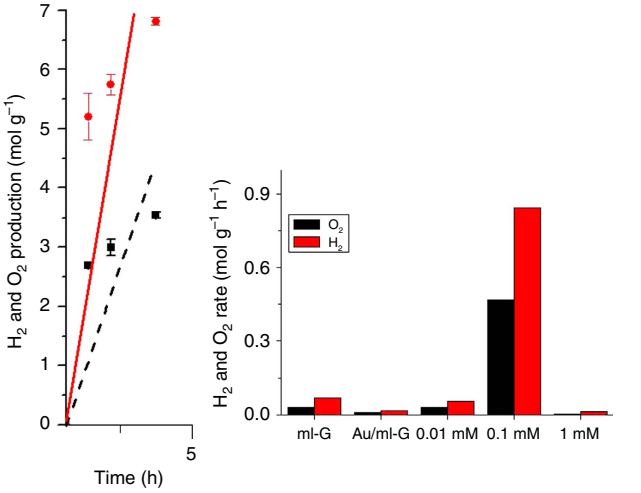

Figure 6 | Photocatalytic H_2 and O_2 production. Temporal evolution of H_2 and O_2 evolution in mols per total mass of photocatalyst on irradiation of Ar-purged MilliQ water in contact with $\overline{Au}$/*ml*-G (Au content 1 μg × cm^{-2}, total photocatalyst content 4.25 μg cm^{-2}). The plot shows the H_2 and O_2 production with the estimated s.d. (calculated as the square root of the sum of (a-ā)^2, being a the value of the data set and ā the mean of the data set, divide by the number of data points). Photocatalytic H_2 and O_2 production rate of various materials for overall water splitting under the same conditions: *ml*-G (G content 3.25 μg cm^{-2}), *Au/ml*-G (unoriented, Au content 30.6 μg, total photocatalyst content 30.6 mg) and $\overline{Au}$/*ml*-G (Au content 1 μg × cm^{-2}, total photocatalyst content 4.25 μg cm^{-2}).

The influence of Au loading on the photocatalytic activity of $\overline{Au}$/*ml*-G was determined by comparing H_2 production rate of three samples prepared under the same conditions, but differing in about one order of magnitude the Au content (0.2, 1.0 and 13.5 μg cm^{-2}, while the G content was constant at 3.25 μg cm^{-2}). The results are also presented in Fig. 6, where the temporal profile of H_2 and O_2 evolution for the most efficient photocatalyst is also presented. Supplementary Fig. 6 presents the temporal profile of the set of samples. As it can be seen in these figures, the sample containing an intermediate Au loading was the one exhibiting the highest photocatalytic efficiency for overall water splitting, decreasing in activity for lower or higher Au contents. The existence of an optimal Au loading can be understood by the contribution of two opposite effects. On one hand, higher Au loading would play a positive effect, increasing the catalytic activity and light-harvesting role of Au. On the other hand, high loadings are unfavourable by increasing Au particle size and G surface coverage.

To determine if the remarkable overall water splitting of $\overline{Au}$/*ml*-G derives from the preparation procedure that is responsible for a strong Au-G interaction and the presence of facet oriented 111 Au nanoplatelets, control experiments using as photocatalysts *Au*/*ml*-G and *ml*-G were also performed. The results are also presented in Fig. 6.

It is worth noting that even in the absence of Au, *ml*-G has a residual overall water-splitting activity under ultraviolet irradiation. Importantly, comparison of the photocatalytic activity of $\overline{Au}$/*ml*-G with that of an analogous sample containing unoriented Au NPs, *Au*/*ml*-G, shows that Au/*ml*-G exhibits even lower catalytic activity than *ml*-G. This indicates that in this sample prepared by adsorbing Au NPs on preformed G, unoriented Au NPs are disfavouring somewhat the overall water splitting and that the characteristic features of $\overline{Au}$/*ml*-G films what determines its remarkable photocatalytic activity in overall water splitting.

Discussion

In view of prior characterization, we propose that the remarkable enhancement of photocatalytic activity for $\overline{Au}$/*ml*-G with respect to the other samples containing or not Au is the result of the one-step pyrolytic preparation procedure that produces a strong Au-G grafting and preferential (111) facet orientation of Au with nanoplatelet morphology. In the literature there is an ample number of precedents showing that graphenes in minor amounts can increase the photocatalytic activity of TiO_2 and other metal oxide semiconductors, a fact that has been attributed to the increase of charge separation by electron migration from the semiconductor conduction band to the G (ref. 39). In recent precedents, multiple-step preparation of Au NPs without any preferential orientation deposited on G/TiO_2 nanocomposites without strong grafting have reported H_2 production rates around 1 mmol per $g_{composite}$ per h under ultraviolet–visible irradiation in the presence of methanol as sacrificial electron donor[40,41]. In the present case, the strong interaction of oriented Au nanoplatelets and graphene can lead to an efficient charge separation disfavouring e^-/h^+ recombination by prompt migration of e^- to *ml*-G. The strong Au-G interaction is experimentally supported by the relatively small average particle size of Au nanoplatelets in spite of the prolonged treatment at elevated pyrolysis temperature (900 °C for 2 h), the shift in XPS of 1.4 eV in the Au 4f binding energy, the complete removal of N from G and occurrence of preferential morphology maximizing the contact area between nanoplatelets and graphene.

To gain understanding on the operation of the photocatalytic mechanism, and particularly the role of Au nanoplatelets, the photoaction spectrum for $\overline{Au}$/*ml*-G was determined by studying the overall water splitting activity of $\overline{Au}$/*ml*-G in the absence of any sacrificial donor using monochromatic light in the range from 300 to 600 nm. The results are presented in Fig. 7.

As it can be seen there, the photocatalytic activity has a clear relative minimum in the 350–450 nm exhibiting the maximum H_2 generation activity at about 550 nm in the visible region. This photoaction spectrum of *Au*/*ml*-G agrees very well with the plasmon band of Au nanoplatelets (Supplementary Fig. 7). Thus, the photoaction spectrum not only proves the photocatalytic activity of *Au*/*ml*-G under visible light irradiation but also provides a strong support that Au nanoplatelets can act as light-harvesting units leading to charge separation. Moreover, a control using a 400-nm cutoff filter shows that *ml*-G in the absence of Au nanoplatelets does not exhibit photocatalytic activity in the visible region. This lack of visible light photocatalytic activity contrasts with the photocatalytic activity data shown in Fig. 6 for ultraviolet–visible light irradiation of *ml*-G that should be attributed to the ultraviolet zone of the irradiation light.

The use of monochromatic light allows determining the apparent quantum yield (Φ) for the overall water splitting that was 0.08% at 300 nm. Although this apparent Φ_{300} value is still low, it is similar to the one that reported for H_2 evolution using Pt-containing g-C_3N_4 using triethanolamine as sacrificial electron donor[20] and about two orders of magnitude higher than that for O_2 evolution with the RuO_2-modified g-C_3N_4 photocatalyst in the presence of Ag^+ as sacrificial electron acceptor[20]. Note that in the present case, Φ_{300} 0.08% corresponds to the overall water splitting in the absence of any additive.

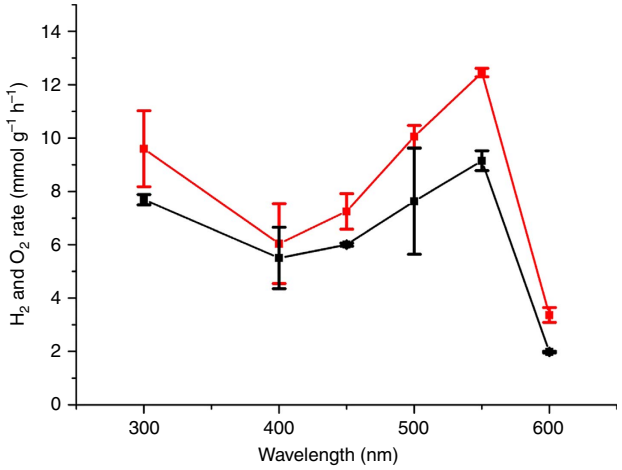

Figure 7 | Photoresponse spectrum referred to the total photocatalyst amount. H_2 (red) and O_2 (black) production rates for *Au*/*ml*-G (Au content 1 μg cm^{-2}, total photocatalyst content 4.25 μg cm^{-2}) with estimated errors (calculated as the square root of the sum of $(a-\bar{a})^2$, being a the value of the data set and $\bar{a}$ the mean of the data set, divide by the number of data points) using monochromatic light (150-W Xe lamp). Irradiation time: 6 h. Note that the production rate is presented in mmol per $g_{composite}$ per h due to the much lower power when irradiating with monochromatic light.

Considering that *ml*-G exhibits also some residual for overall water splitting, a possible photocatalytic mechanism for ultraviolet–visible light irradiation of *Au*/*ml*-G films is proposed in Fig. 8. In this Fig. 8, G would show two different roles. On one hand, G could present photocatalytic activity on absorption of ultraviolet photons, with fast e^-/h^+ recombination. On the other hand, visible light can only excite Au nanoplatelets, promoting charge separation with electron migration from Au nanoplatelets to G that in this case would act as enhancer of the charge separation.

To provide some evidence to this proposal, the energy of electrons in the valence band was measured by ultraviolet photoelectron spectroscopy (UPS) spectroscopy for *Au*/*ml*-G films. The valence band energy of *Au*/*ml*-G is presented in Supplementary Fig. 8 and it agrees with some minor changes with that previously reported for graphenes[42]. These minor changes could correspond to the levels modified or introduced by Au nanoplatelets. Extrapolation of the onset of valence band electrons gives an estimation of 1.5 V as the potential of holes in *Au*/*ml*-G films. This value would make the process of H_2O oxidation to O_2 thermodynamically feasible.

In a different study trying to determine the location of h^+, oxidation of Pb^{2+} to PbO_2 was carried out in aqueous solution on *Au*/*ml*-G films using either Ce^{IV} and O_2 as sacrificial electron acceptors. Subsequent determination of the presence of PbO_2 by electron microscopy EDX analysis combined with EBSD and imaging by FESEM showed that the element Pb (EDX) in the crystal form corresponding to PbO_2 (EBSD) was present on present on top of Au nanoplatelets, but Pb was below the detection limit on G. It should be, however, noted the different resolution of the microscopy techniques. Thus, while EDX has higher resolution and locates Pb on Au, electron diffraction has lower resolution than Au nanoplatelets. Methods section provides a detailed description of the experimental conditions, and Supplementary Figs 9 and 10 shows images indicating that oxidation occurs exclusively on the Au nanoplatelets, but not on the G surface.

In conclusion, herein it has been shown that films of nanometric thickness consisting in 111 facet-oriented Au nanoplatelets strongly grafted on *ml*-G are extremely efficient for the photocatalytic overall water splitting in to H_2 and O_2 in the absence of sacrificial electron donor with maximal production rate values of 1.2 mol_{H2} per $g_{composite}$ per h. *Au*/*ml*-G films exhibit even visible light photoresponse arising from the plasmon band of Au NPs. The estimated oxidation potential of valence band h^+ is 1.5 V and electron microscopy shows the photodeposition of PbO_2 exclusively on Au nanoplatelets. Further work should be aimed to gain deeper understanding on the interaction of Au nanoplatelets and G and to the optimization of the photocatalytic activity of these materials by alloying and doping.

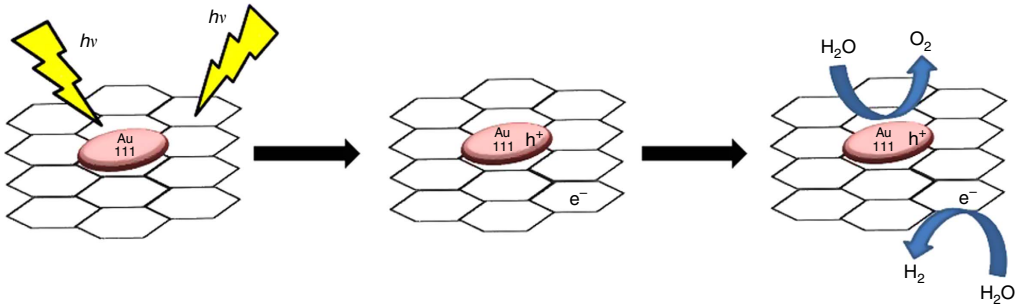

Figure 8 | Proposed mechanism. Proposed mechanism for the photocatalytic reaction of water splitting.

Methods

Materials. All reagents used in this work were purchased from Sigma Aldrich and were used as received without further purification.

Preparation of *Au*/*ml*-G films. The (111) oriented Au nanoparticles supported on *ml*-G film were prepared as reported before[29]. Briefly, an aqueous solution of chitosan (500 mg of chitosan in 25 ml of water) was spin coated onto $2 \times 2\,cm^2$ quartz substrates and dried. Quartz substrates were immersed into 1, 0.1 and 0.01 mM $HAuCl_4$ aqueous solutions for 1 min to favour metal absorption on the film surface. After drying at 100 °C, the thin films were pyrolysed under Ar atmosphere at 900 °C.

Estimation of the graphene mass in *Au*/*ml*-G films. The mass of graphene in nanometric *Au*/*ml*-G films was calculated following two alternative procedures:

On the basis of the weight of the chitosan precursor: the mass of an aqueous solution of chitosan (2 wt%) deposited onto a quartz substrate by spin coating was determined with a balance with 0.1 mg nominal precision by difference between the quartz substrate with and without the solution film. Thermogravimetric analysis shows that during the pyrolysis process at 900 °C a mass reduction of 60% takes place in the transformation of chitosan into graphene. Knowing the mass of solution deposited onto a $2 \times 2\text{-}cm^2$ quartz substrate, the chitosan content (2 wt%) and the mass reduction in the pyrolysis, the weight of the residual graphene can be estimated by applying the equation $0.02 \times 0.6 \times$ mass of the solution. In this way, most of the experiments were performed with films containing an estimated mass of 13 μg of graphene in $2 \times 2\text{-}cm^2$ films.

On the basis of density value and volume: estimated values of graphene density range between 1.5 and 2 $g\,cm^{-3}$. Since our films are typically 4 cm^2 and the film thickness determined by AFM was 20 nm, a volume of $8 \times 10^{-6}\,cm^{-3}$ is calculated. By multiplying density per volume an estimation of the graphene mass can be obtained. Thus, these calculations estimate that the graphene mass in $2 \times 2\text{-}cm^2$ films should be between 12 and 16 μg.

HR-TEM images and EBSD. TEM images of an oriented *Au*/*ml*-G sample were recorded at the Electron Microscopy Center of the Universitat de Valencia after abrasion of the quartz support by consecutive treatments consisting in mechanical polishing from the back side of the substrate until ~100-μm thickness, followed by backside dimpling with a dimple grinder GATAN Model 656 and final low-angle, ion milling using an argon gun and plishing system Fishione Model 1,010. The fundamentals and detailed description of the methodology is described elsewhere[43].

UPS valence band measurement of *Au*/*ml*-G. Ultraviolet photoemission measurements (UPS) were carried out in an ultra-high-vacuum ESCALAB 210 multianalysis system (base pressure 1.0×10^{-10} mbar) from Thermo VG Scientific. Photoelectrons were excited by means of a helium lamp by using the He II (40.8 eV) excitation lines. UPS spectra have been referred to the Fermi level (E_F). Previously to these measurements, samples were introduced in the analysis chamber and sputtered by using an Ar^+ gun for 2 min, to clean the surface, removing adsorbates. Assignment of the energy peaks has been made based on the values previously reported in the literature[42].

Photodepostion of PbO_2 by oxidation of $Pb(OAc)_2$. A $1 \times 1\text{-}cm^2$ *Au*/*ml*-G film was placed into a quartz cuvette. Then, 1.5 ml of a 1 mM aqueous solution $Pb(OAc)_2$ and another 1.5 ml of a 1 mM aqueous solution of $Ce(NH_4)_2(NO_3)_6$ were introduced inside the cuvette. The cuvette was capped with a rubber septum and the aqueous phase purged with argon for 15 min before irradiation. The cuvette was irradiated with the Xe lamp for 1 h. After this time, the *Au*/*ml*-G film was recovered, exhaustively washed with MilliQ water and studied by HRTEM and EDX to determine the location of Pb on the film.

In an additional experiment $1 \times 1\text{-}cm^2$ *Au*/*ml*-G film was placed into a quartz cuvette adding 1.5 ml of a 1-mM aqueous solution $Pb(OAc)_2$. The cuvette was open to the ambient and submitted to 3-h Xe lamp irradiation. After this time, the *Au*/*ml*-G film was recovered, exhaustively washed with MilliQ water and studied by scanning electron microscopy, EDX and EBSD looking for the most intense peaks corresponding to PbO_2, PbO and Pb. The images are presented in Supplementary Fig. 10.

Photocatalytic hydrogen production tests. The *Au*/*ml*-G films were introduced in a close reactor and Ar-purged water was spread on top of the film until complete film coverage. Experiments with TEOA as sacrificial agent were carried out with Ar-purged water with a 15% w/v of TEOA. The H_2 evolution tests were carried out in a 300-ml aluminium reactor with a quartz window connected to an Agilent 490 Micro GC (Molsieve 5A column with Ar as carrier gas) and irradiated with a 300-W Xe lamp. The experiments performed under monochromatic irradiation were carried out with a 150-W Xenon lamp through a Czerny Turner monochromator. The temperature and pressure inside the reactor was controlled through a thermocouple and a manometer, respectively.

Data availability. All relevant data are available from the authors.

References

1. Lv, X. J., Zhou, S., Huang, X., Wang, C. & Fu, W. F. Photocatalytic overall water splitting promoted by SnOx-$NiGa_2O_4$ photocatalysts. *Appl. Cat. B: Environ.* **182,** 220–228 (2016).
2. Xu, J., Wang, L. & Cao, X. Polymer supported graphene-CdS composite catalyst with enhanced photocatalytic hydrogen production from water splitting under visible light. *Chem. Eng. J.* **283,** 816–825 (2016).
3. Tanigawa, S. & Irie, H. Visible-light-sensitive two-step overall water-splitting based on band structure control of titanium dioxide. *Appl. Cat. B: Environ.* **180,** 1–5 (2016).
4. Maeda, K. *et al.* GaN:ZnO solid solution as a photocatalyst for visible-light-driven overall water splitting. *J. Am. Chem. Soc.* **127,** 8286–8287 (2005).
5. Maeda, K. *et al.* Photocatalyst releasing hydrogen from water. *Nature* **440,** 295 (2006).
6. Kato, H. & Kudo, A. Visible-light-response and photocatalytic activities of TiO2 and SrTiO3 photocatalysts codoped with antimony and chromium. *J. Phys. Chem. B* **106,** 5029–5034 (2002).
7. Xiang, Q., Cheng, B. & Yu, J. Graphene-based photocatalysts for solar-fuel generation. *Angew. Chem. Int. Ed.* **54,** 11350–11366 (2015).
8. Navalon, S., Dhakshinamoorthy, A., Alvaro, M. & Garcia, H. Carbocatalysis by graphene-based materials. *Chem. Rev.* **114,** 6179–6212 (2014).
9. Yu, J., Jin, J., Cheng, B. & Jaroniec, M. A noble metal-free reduced graphene oxide-cds nanorod composite for the enhanced visible-light photocatalytic reduction of CO2 to solar fuel. *J. Mat. Chem. A* **2,** 3407–3416 (2014).
10. Meng, F., Cushing, S. K., Li, J., Hao, S. & Wu, N. Enhancement of solar hydrogen generation by synergistic interaction of La2Ti2O7 photocatalyst with plasmonic gold nanoparticles and reduced graphene oxide nanosheets. *ACS Catal.* **5,** 1949–1955 (2015).
11. Shown, I. *et al.* Highly efficient visible light photocatalytic reduction of co2 to hydrocarbon fuels by cu-nanoparticle decorated graphene oxide. *Nano Lett.* **14,** 6097–6103 (2014).
12. Shang, L. *et al.* Graphene-supported ultrafine metal nanoparticles encapsulated by mesoporous silica: robust catalysts for oxidation and reduction reactions. *Angew. Chem. Int. Ed.* **53,** 250–254 (2014).
13. Latorre-Sánchez, M., Primo, A. & García, H. P-doped graphene obtained by pyrolysis of modified alginate as a photocatalyst for hydrogen generation from water-methanol mixtures. *Angew. Chem. Int. Ed.* **52,** 11813–11816 (2013).
14. Lavorato, C., Primo, A., Molinari, R. & Garcia, H. N-doped graphene derived from biomass as a visible-light photocatalyst for hydrogen generation from water/methanol mixtures. *Chem. - A Eur. J.* **20,** 187–194 (2014).
15. Shams, S. S., Zhang, L. S., Hu, R., Zhang, R. & Zhu, J. Synthesis of graphene from biomass: a green chemistry approach. *Mater. Lett.* **161,** 476–479 (2015).
16. Meng, F. *et al.* Biomass-derived high-performance tungsten-based electrocatalysts on graphene for hydrogen evolution. *J. Mater. Chem. A* **3,** 18572–18577 (2015).
17. Vilatela, J. J. & Eder, D. Nanocarbon composites and hybrids in sustainability: a review. *ChemSusChem* **5,** 456–478 (2012).
18. Rani, P. & Jindal, V. K. Designing band gap of graphene by B and N dopant atoms. *RSC Adv.* **3,** 802–812 (2013).
19. Zheng, Y. *et al.* Hydrogen evolution by a metal-free electrocatalyst. *Nat. Commun.* **5,** 3783 (2014).
20. Wang, X. *et al.* A metal-free polymeric photocatalyst for hydrogen production from water under visible light. *Nat. Mater.* **8,** 76–80 (2009).
21. Huang, H., Yang, S., Vajtai, R., Wang, X. & Ajayan, P. M. Pt-decorated 3D architectures built from graphene and graphitic carbon nitride nanosheets as efficient methanol oxidation catalysts. *Adv. Mater.* **26,** 5160–5165 (2014).
22. Shiraishi, Y. *et al.* Platinum nanoparticles strongly associated with graphitic carbon nitride as efficient co-catalysts for photocatalytic hydrogen evolution under visible light. *Chem. Commun.* **50,** 15255–15258 (2014).
23. G. Baldoví, H. *et al.* Visible-light photoresponse of gold nanoparticles supported on TiO2: A combined photocatalytic, photoelectrochemical, and transient spectroscopy study. *ChemPhysChem* **16,** 335–341 (2015).
24. Serra, M., Albero, J. & Garcia, H. Photocatalytic Activity of Au/TiO2 photocatalysts for H-2 evolution: role of the Au nanoparticles as a function of the irradiation wavelength. *ChemPhysChem* **16,** 1842–1845 (2015).
25. Gomes Silva, C., Juárez, R., Marino, T., Molinari, R. & García, H. Influence of excitation wavelength (UV or visible light) on the photocatalytic activity of titania containing gold nanoparticles for the generation of hydrogen or oxygen from water. *J. Am. Chem. Soc.* **133,** 595–602 (2011).
26. El Kadib, A. Chitosan as a sustainable organocatalyst: a concise overview. *ChemSusChem* **8,** 217–244 (2015).

27. Primo, A., Atienzar, P., Sanchez, E., Delgado, J. M. & García, H. From biomass wastes to large-area, high-quality, N-doped graphene: catalyst-free carbonization of chitosan coatings on arbitrary substrates. *Chem. Commun.* **48,** 9254–9256 (2012).
28. Primo, A. & Quignard, F. Chitosan as efficient porous support for dispersion of highly active gold nanoparticles: design of hybrid catalyst for carbon-carbon bond formation. *Chem. Commun.* **46,** 5593–5595 (2010).
29. Primo, A. *et al.* One-step pyrolysis preparation of 1.1.1 oriented gold nanoplatelets supported on graphene and six orders of magnitude enhancement of the resulting catalytic activity. *Angew. Chem. Int. Ed.* **54,** 1–7 (2015).
30. Lalov, I. G., Guerginov, I. I., Krysteva, M. A. & Fartsov, K. Treatment of waste water from distilleries with chitosan. *Water Res.* **34,** 1503–1506 (2000).
31. No, H. K. & Meyers, S. P. *Application of Chitosan for Treatment of Wastewaters in Reviews of Environmental Contamination and Toxicology: Continuation of Residue Reviews*. (eds George, W. W.) 1–27 (Springer, 2000).
32. Liu, C. *et al.* Hydrothermal synthesis of N-doped TiO2 nanowires and N-doped graphene heterostructures with enhanced photocatalytic properties. *J. Alloys Compd.* **656,** 24–32 (2016).
33. Radnik, J., Mohr, C. & Claus, P. On the origin of binding energy shifts of core levels of supported gold nanoparticles and dependence of pretreatment and materials synthesis. *Phys. Chem. Chem. Phys.* **5,** 172–177 (2003).
34. Primo, A. *et al.* High catalytic activity of oriented 2.0.0 copper(I) oxide grown on graphene film. *Nat. Commun.* **6,** 8561 (2015).
35. Abbasi, M. *et al.* Application of transmitted Kikuchi diffraction in studying nano-oxide and ultrafine metallic grains. *ACS Nano* **9,** 10991–11002 (2015).
36. Trimby, P. T. Orientation mapping of nanostructured materials using transmission kikuchi diffraction in the scanning electron microscope. *Ultramicroscopy* **120,** 16–24 (2012).
37. Johnson, C. J., Dujardin, E., Davis, S. A., Murphy, C. J. & Mann, S. Growth and form of gold nanorods prepared by seed-mediated, surfactant-directed synthesis. *J. Mater. Chem.* **12,** 1765–1770 (2002).
38. Ikeda, S. *et al.* Mechano-catalysis—a novel method for overall water splitting. *Phys. Chem. Chem. Phys.* **1,** 4485–4491 (1999).
39. Khalid, N. R., Ahmed, E., Hong, Z., Sana, L. & Ahmed, M. Enhanced photocatalytic activity of graphene-TiO_2 composite under visible light irradiation. *Curr. Appl. Phys.* **13,** 659–663 (2013).
40. Singh, G. P., Shrestha, K. M., Nepal, A., Klabunde, K. J. & Sorensen, C. M. Graphene supported plasmonic photocatalyst for hydrogen evolution in photocatalytic water splitting. *Nanotechnology* **25,** 265701 (2014).
41. Wang, M., Han, J., Xiong, H. & Guo, R. Yolk@shell nanoarchitecture of Au@r-GO/TiO2 hybrids as powerful visible light photocatalysts. *Langmuir* **31,** 6220–6228 (2015).
42. Luo, Z. *et al.* Modulating the electronic structures of graphene by controllable hydrogenation. *Appl. Phys. Lett.* **97,** 233111 (2010).
43. Sridhara Rao, D. V., Muraleedharan, K. & Humphreys, C. J. in *Microscope Science, Technology, Applications and Education* **3,** 1232–1244 (Formatec (2010).

Acknowledgements

Financial support by the Spanish Ministry of Economy and Competitiveness (Severo Ochoa and CTQ2012-32315) and Generalitat Valenciana (Prometeo 2013-019) is gratefully acknowledged. D.M. and I.E.-A. thank to Spanish Ministry of Science for PhD scholarships.

Author contributions

A.P. discovered the orientation of Au nanoplatelets, performed the characterization and wrote part of the manuscript; J.A. supervised the photocatalytic experiments and wrote part of the manuscript; D.M. performed the photocatalytic experiments and determination of the location of PbO_2 on $\overline{Au}/ml$-G films; I.E.-A. prepared the materials and assisted sample characterization; participation of J.F.S.R. was exclusively UPS measurement of $\overline{Au}/ml$-G films; H.G. supervised the research and wrote most of the manuscript. All the authors discussed the results and corrected the article draft.

Additional information

Supplementary Information accompanies this paper at http://www.nature.com/naturecommunications

Competing financial interests: A patent protecting the intellectual property on the photocatalytic activity of these materials based on oriented metal nanoparticles supported on graphene for hydrogen generation has been applied in the patent office. Fotocatalizador a base de grafeno para la producción de combustibles solares (23/02/2016) P201630203.

Reprints and permission information is available online at http://npg.nature.com/reprintsandpermissions/

How to cite this article: Mateo, D. *et al.* 111 oriented gold nanoplatelets on multilayer graphene as visible light photocatalyst for overall water splitting. *Nat. Commun.* 7:11819 doi: 10.1038/ncomms11819 (2016).